energies

MDPI

Article

Piezoelectric Properties of PVDF-Zn_2GeO_4 Fine Fiber Mats

Fariha Rubaiya [1], Swati Mohan [2], Bhupendra B. Srivastava [2], Horacio Vasquez [1] and Karen Lozano [1,*]

[1] Department of Mechanical Engineering, University of Texas Rio Grande Valley, Edinburg, TX 78539, USA; fariha.rubaiya01@utrgv.edu (F.R.); horacio.vasquez@utrgv.edu (H.V.)
[2] Department of Chemistry, University of Texas Rio Grande Valley, Edinburg, TX 78539, USA; swati.mohan01@utrgv.edu (S.M.); bhupendra.srivastava@utrgv.edu (B.B.S.)
* Correspondence: karen.lozano@utrgv.edu

Abstract: The current paper presents the development and characterization of polyvinylidene fluoride (PVDF)-Zn_2GeO_4 (ZGO) fine fiber mats. ZGO nanorods (NRs) were synthesized using a hydrothermal method and incorporated in a PVDF solution to produce fine fiber mats. The fiber mats were prepared by varying the concentration of ZGO NRs (1.25–10 wt %) using the Forcespinning® method. The developed mats showed long, continuous, and homogeneous fibers, with average fiber diameters varying from 0.7 to 1 µm, depending on the ZGO concentration. X-ray diffraction spectra depicted a positive correlation among concentration of ZGO NRs and strengthening of the beta phase within the PVDF fibers. The composite system containing 1.25 wt % of ZGO displayed the highest piezoelectric response of 172 V. This fine fiber composite system has promising potential applications for energy harvesting and the powering of wearable and portable electronics.

Keywords: PVDF; Zn_2GeO_4; Forcespinning; piezoelectric; fibers

check for updates

Citation: Rubaiya, F.; Mohan, S.; Srivastava, B.B.; Vasquez, H.; Lozano, K. Piezoelectric Properties of PVDF-Zn_2GeO_4 Fine Fiber Mats. *Energies* **2021**, *14*, 5936. https://doi.org/10.3390/en14185936

Academic Editor: Vijay Kumar Thakur

Received: 16 August 2021
Accepted: 14 September 2021
Published: 18 September 2021

Publisher's Note: MDPI stays neutral with regard to jurisdictional claims in published maps and institutional affiliations.

Copyright: © 2021 by the authors. Licensee MDPI, Basel, Switzerland. This article is an open access article distributed under the terms and conditions of the Creative Commons Attribution (CC BY) license (https://creativecommons.org/licenses/by/4.0/).

1. Introduction

Wearable and portable electronics are now considered a necessity, given their contribution to the development of human interactive applications in areas such as biomedicine, aeronautics, and agriculture [1]. Research and development teams are eagerly working toward the development of smaller, inexpensive, lighter, and highly efficient wearable and portable electronics. Energy harvested from sunlight, thermal, and chemical sources can power most routine activities in our daily life. However, powering small electronic devices such as micropumps, sensors, pacemakers, and personal portable electronics using the abovementioned sources is still a challenge given the intrinsic limitations of batteries. Traditional batteries have limited life spans and storage capacities, lack an environmentally friendly nature, and require frequent recharging [2,3]. Hence, self-powered technology can be a great solution to overcome these challenges [4]. There are several promising methods that can be used to provide energy to electronic devices, such as piezoelectric, electrostatic, electromagnetic, and triboelectric energy harvesting methods [5–8]. Among all these sources, piezoelectricity is highly promising given its ability to produce an electrical response from simple mechanical stress. As mechanical energy is the most abundant energy in our environment, motion-based energy harvesting devices capable of producing energy from mechanical motion such as mechanical vibrations, pressure, or periodic motions are an attractive alternative for developing self-powered systems [9]. The main advantage of piezoelectricity over thermal and solar harvesting is that ambient vibrations are often persistent due to the operational conditions of a system, and it does not depend on unsteady and unpredictable environmental conditions, which can vary with time [10]. Hence, in recent times, much focus has been given to piezoelectric energy harvesting as it converts dynamic mechanical energy into electrical energy using piezoelectric materials.

Piezoelectricity has been detected in numerous materials, and has been adopted using piezoelectric ceramic single crystals (i.e., lead magnesium niobate-lead zirconate

titanate [11], lead magnesium niobate-lead titanate [12], and lead magnesium niobate-lead zirconate titanate-manganese doped [13]), lead-free piezoelectric systems (i.e., potassium sodium niobate-bismuth sodium zirconate-silver antimony oxide-ferrite [14] and manganese-modified potassium sodium niobate [15]), high-temperature piezoelectric systems (i.e., bismuth ferrite-bismuth tantalum titanate [16] and bismuth ferrite-barium titanate [17]), and ZnO nanowires [18], to mention some. However, these materials are usually brittle and possess high density. To overcome these problems, researchers have developed piezoelectric composites consisting of an active piezoceramic phase embedded in polymeric matrices that have piezoelectric properties such as polyvinylidene fluoride (PVDF), polyvinylidene fluoride-trifluoro ethylene (PVDF-TrFE), polyamides (PA), and polylactic acids (PLA) [19].

Among the abovementioned polymers, PVDF has shown strong potential in energy harvesting due to its light weight, flexibility, durability, chemical stability, affordability, and high voltage output when strained [20]. Semicrystalline PVDF [21–23] and its copolymers, such as polyvinylidene fluoride-co-hexafluoropropylene (PVDF-HFP), are widely used in piezoelectric systems [24]. PVDF is a polymorphic system that exists in different conformation phases, where each one has a unique set of properties. The semi-crystalline structure of PVDF is known for having five crystalline phases: α, β, δ, γ, and ε [25]. α and β are the most prevailing phases, where α is a non-polar phase, while the β phase is polar and mostly responsible for its piezoelectric response [26]. There are several procedures for the conversion of α phase to β phase, such as melt methods [27], solvent methods [28], mechanical stretching [29], copolymerization [30], and the addition of fillers [31]. Incorporation of certain fillers such as $BaTiO_3$ [32], TiO_2 [33], ferrite [34], silver [35], graphene [36], and carbon nanotubes [37] has also been known to aid in the development of electroactive phases within PVDF.

Conventional fiber-making methods promote a high degree of mechanical stretching, and are therefore highly sought after in the development of piezoelectric systems. Electrospinning and centrifugal spinning or Forcespinning® (FS) of piezoelectric-based polymeric systems have been widely used. Fibers developed through electrospinning have been vastly reported in the literature since the method was shown to produce nano- and single-digit microfibers in the late 1980s. Studies have shown that electrospinning can effectively produce piezoelectric PVDF fibers with enhanced β-phase contents by stretching the polymer solution into solid fibrils [20]. However, electrospinning has some limitations, such as the need for high electric field strength and low output. To overcome the drawbacks of electrospinning, Sarkar et al. developed the FS method in the 2000s, in which centrifugal force is used to produce fine fibers instead of an electrical field [38]. In the FS method, the angular velocity of a spinneret forces the molten system or solution through small orifices within the rotating spinneret. The material exits the spinneret and stretches into fibers as the system rotates, all in the absence of an electric field, therefore broadening the type of materials that can be used to develop fibrils, since the dielectric constant is not a parameter that must be considered. Variables of importance in the FS system are the intrinsic properties (e.g., viscoelasticity and surface tension) of the chosen material, and processing parameters such as angular velocity, size of the exit nozzle, concentration of solute in solvent (or temperature of the melt), humidity of the environment, and distance to the collector. The developed fluid jets follow highly curved trajectories and undergo stretching and evaporation of the used solvent or cooling (molten systems), and developed fibers are finally deposited in the vertical collector (laboratory-scale system) or horizontal conveyor belt (industrial-scale system).

Metal oxides (such as ZnO, TiO_2, and FeO) used as fillers in polymer matrices have also been reported to enhance the piezoelectric response [1,39,40]. Ternary metal oxides can retain multiple oxidation states that allow for multiple redox reactions. They appear to be the most promising materials for pseudo-capacitors, as they are known for showing a higher super-capacitive performance than single-component metal oxides [41]. Germanates A_2GeO_4 (A = Ca, Sr, Ba, Zn, etc.) have recently gained attention due to their

catalytic and optical properties, as well as for their eco-friendliness, stability, and availability [42]. As a low-cost ternary oxide, Zn_2GeO_4 (ZGO) has been shown to possess exciting properties that make it a promising candidate for applications needing negative thermal expansion materials, as well as in optoelectronics, chemical and electrochemical sensors, catalysis, lithium/sodium batteries, and electroluminescence devices [39,40,42–46]. It is a typical n-type semiconductor with a wide band gap of 4.4 eV, high excitonic binding energy (EBE), stable phenakite crystalline structure, and excellent thermal and chemical stability [39,40,43]. These properties are more significanct when ZGO is synthesized with a well-defined nano-domain morphology (such as nanorods). It also exhibits high wavelength selectivity in UV photodetectors with fast response and recovery times, and bright white-bluish luminescence [47].

Even though ZGO has been used in various applications given its electrochemical properties and high theoretical capacity, its effect on piezoelectric response has rarely been explored in the literature. In this study, we developed a composite-based germanate, Zn_2GeO_4, as filler for a PVDF matrix, and its piezoelectric response was analyzed. The main aim of the present work was the synthesis of ZGO nanorods and incorporation of these within a PVDF matrix to subsequently develop fine fiber composites using the FS method. The PVDF-ZGO fiber-based composite provides promising piezoelectric and photoluminescence properties, which may open up a new field where both characteristics are simultaneously utilized. To the best of our knowledge, no previous studies investigated the piezoelectric property of Zn_2GeO_4 NRs-PVDF polymer composites.

2. Experimental Details

2.1. Materials

Zinc nitrate hexahydrate ($Zn(NO_3)_2.6H_2O$, germanium (IV) oxide (GeO_2), and N,N-dimethylacetamide (DMA) were purchased from Sigma-Aldrich (MilliporeSigma). Ammonium hydroxide was purchased from Avantor Performance Materials. Acetone was purchased from Fisher Chemical, and KYNAR 741 (Batch: 19C6001) polyvinylidene fluoride (PVDF) was acquired from Arkema Inc.

2.2. Synthesis of Zn_2GeO_4

ZGO was synthesized using the hydrothermal method [48]. We dissolved 2.0 mmoL of $(Zn(NO_3)_2.6H_2O$ with 1 mmoL of GeO_2 in 15 mL of water, and ammonia solution was added to adjust the pH of the solution to the desired value while stirring for 3–4 h. After the solution was mixed, it was transferred to a 30 mL Teflon-lined stainless-steel autoclave in an ambient environment. The sealed autoclave was heated at 220 °C for 4 h. The sample was then cooled to room temperature, which was followed by purification using centrifugation and repeated washing with a mixture of a water–ethanol solution. The sample was then dried overnight in the oven at 60 °C.

2.3. Synthesis of PVDF-ZGO Fiber Mats

PVDF solutions were prepared by dissolving the polymer in a mixture (1:1) of DMA and acetone. ZGO nanorods were added to these solutions, also at different concentrations (1.25–10 wt % with respect to the polymer). The suspensions were magnetically stirred at 70 °C in a silicon oil bath. Each mixture was stirred for 1.5–2 h at 1000 rpm to obtain homogeneous dispersion. The developed samples were then fed into the spinneret of a Cyclone system (Fiberio Technology Corporation) and spun at 8000 rpm. Figure 1a shows a schematic representation of the FS process.

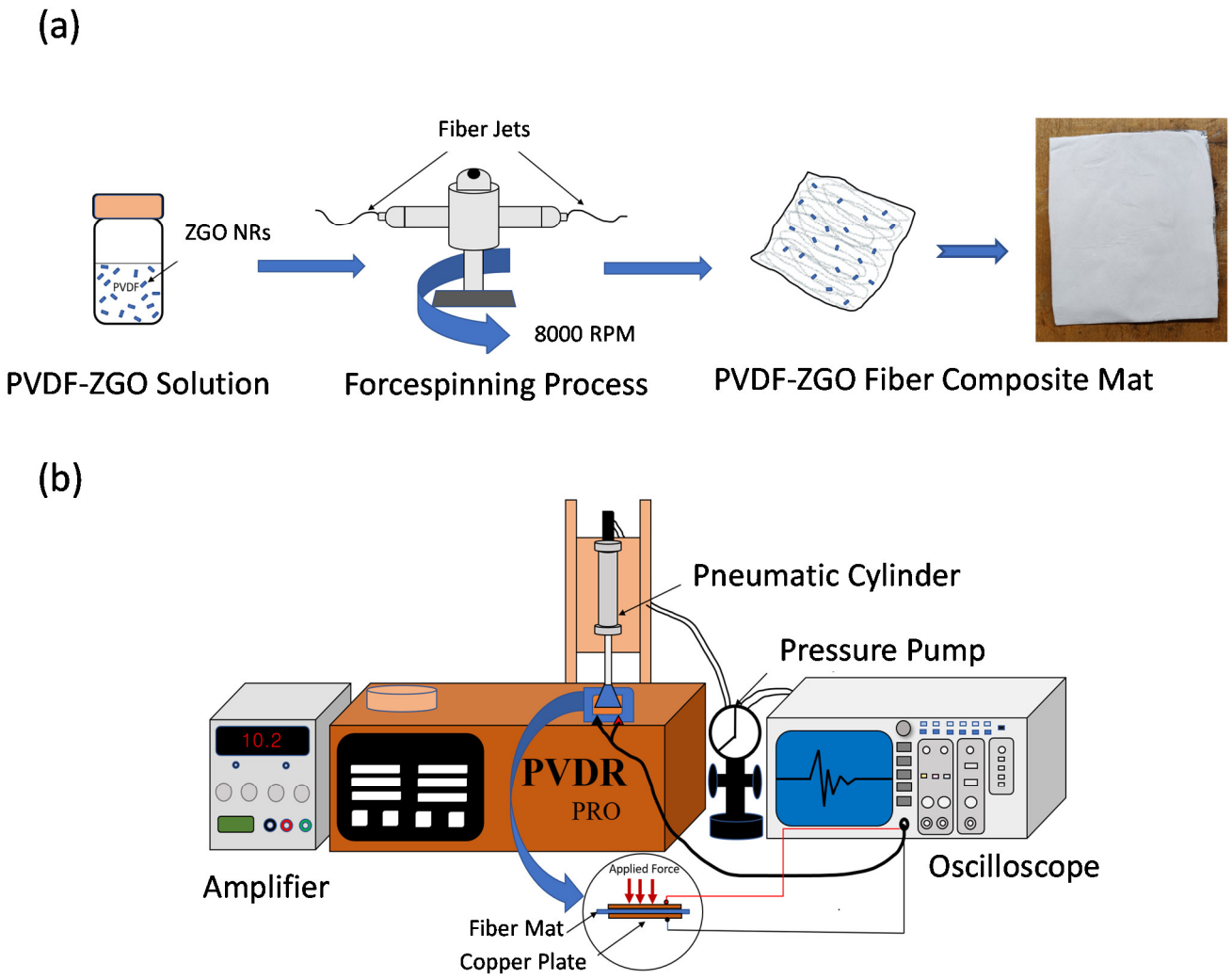

Figure 1. (**a**) Schematic representation of the preparation of ZGO-PVDF fiber composite based mats and (**b**) the pneumatic cylinder and oscilloscope set-up for piezoelectric testing.

2.4. Characterization Techniques

The morphological features of developed fiber-based mats were analyzed using a Zeiss EVO LS10 scanning electron microscope operated at 1–3 kV. An EDAX (Octane Super) was used to conduct energy-dispersive X-ray spectroscopy (EDS) analysis of ZGO NRs and the fiber composites. X-ray diffraction analysis was conducted using a single-axis Bruker D8 Advance X-ray scattering instrument from an effective wavelength of 2θ range from 10° to 80°, in increments of 0.4° at a rate of 2° min^{-1} under a power setting of 40 kV and 40 mA. An Edinburgh Instrument FLS 980 fluorimeter was used for photoluminescence emissions using a steady-state Xenon (Xe) lamp source. Thermogravimetric analysis was performed using a TGAQ-500 at a rate of 5 °C/min from 25 to 1000 °C using samples of 10 mg. Piezoelectric testing was conducted by placing the fiber mat in between two 5 cm × 3 cm copper foil plates working as electrodes. The copper plate was then connected to a Tektronix TDS 2012B Oscilloscope through a Tektronix TPP0101 passive 10× voltage probe (100 MHz bandwidth). The oscilloscope was set to 10× probe attenuation to be on the same scale as the voltage probe. A pneumatic cylinder stroked the specimen with an adjustable force, which was measured using a load cell, with a pressure of 30 psi (206 kPa) at 1.3 Hz. The piezoelectric response was recorded as peak-to-peak voltages at DC coupling by using the oscilloscope-signals. Figure 1b shows a schematic representation of the piezoelectric testing.

3. Results and Discussion

Figure 2a shows the electron micrographs of the developed ZGO nanorods. Figure 2b shows the corresponding EDS spectra, clearly showing the presence of zinc, germanium, and oxygen. Figure 2c shows the corresponding XRD pattern of these ZGO nanorods. The XRD pattern of ZGO correlates with previously reported work [42], and with the respective standard pattern of Zn_2GeO_4 (JCPDS file No. 11-0687), therefore confirming the highly crystalline nature of the developed system.

The XRD for pure PVDF shown in Figure 2d depicts the α phase shown at 2θ = 17.7°, 18.3°, and 26.8° [49], and β-phase characteristics are shown at 2θ at 20.6° [50]. In this same figure, the XRD spectra for the PVDF fibers and its ZGO composites are also presented, with all showing a well-defined hump at exactly 20.6°. This proves that the spun PVDF-ZGO fiber composites had an α phase to β phase transition. This transition of phases happened due to the elongation that occurred in the FS method. PVDF 10 wt % ZGO fiber represents a combination of peaks from ZGO and PVDF. The intensity of ZGO peaks decreases with the decline in ZGO concentration in the system. However, the peak demonstrating the β phase prevailed in all of the PVDF-ZGO fibers.

Figure 3 exhibits SEM images of the PVDF fiber and ZGO-filled PVDF composite fibers, along with the corresponding histograms of fiber diameters. The fibers display a smooth surface morphology; agglomeration of nanorods was not observed. It also shows an unvarying cross-section with a high degree of entanglement, as expected in a nonwoven fiber system such as those previously reported via the FS method [51]. Figure 3a shows an SEM image for PVDF control fibers that are randomly oriented, with an average fiber diameter of 0.7 μm, ranging from 0.3–1.5 μm. Fibers reinforced with ZGO show fiber diameters ranging from 0.2–3 μm, without any correlation with the concentration of ZGO, suggesting that fiber orientation and diameter are dependent on humidity and rotational speed rather than the concentration of nanorods. From the images, it can be seen that pure PVDF fibers (Figure 3a,b), PVDF 1.25 wt % ZGO (Figure 3c,d), and PVDF with 5 wt % ZGO (Figure 3i,j) show long, continuous, and highly aligned fibers with a highly homogeneous surface morphology. The average fiber diameter of the 5 wt % ZGO-PVDF fiber was 0.75 μm, with the lowest standard deviation among all the other fiber systems.

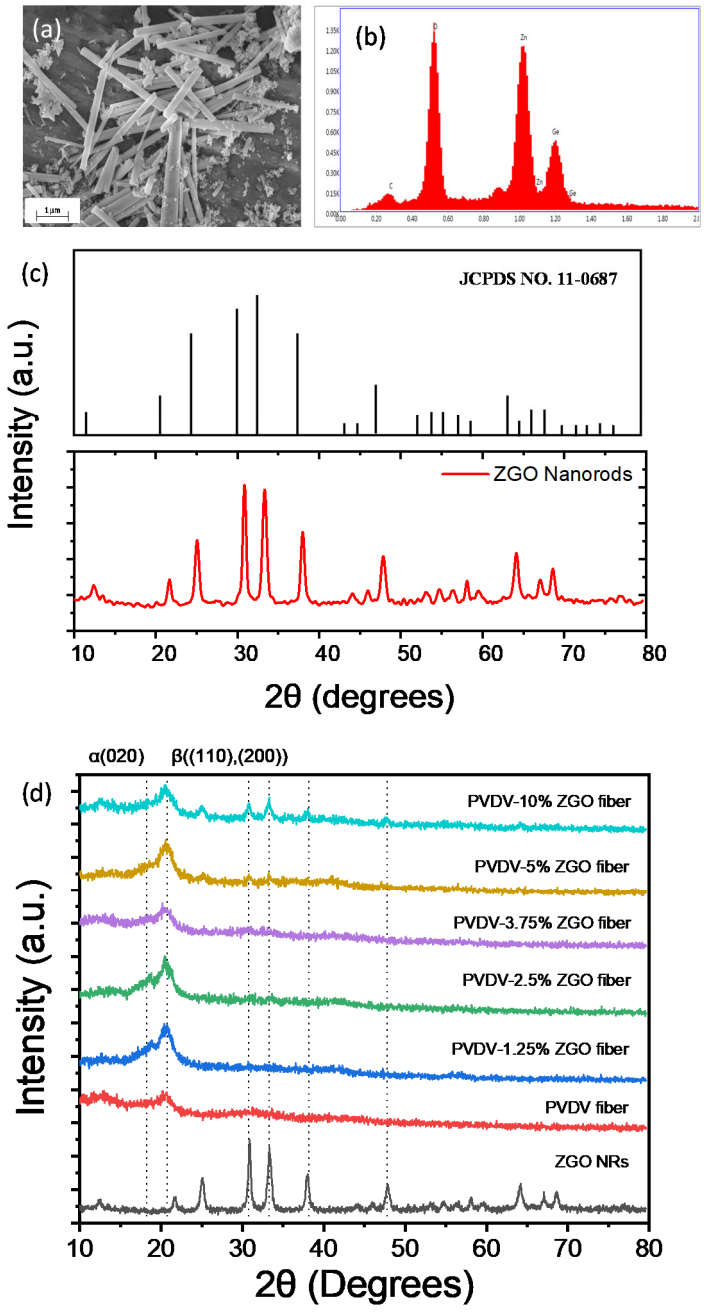

Figure 2. (**a**) SEM micrograph of developed ZGO nanorods, (**b**) EDAX spectra of ZGO nanorods, (**c**) XRD pattern of ZGO nanorods, and (**d**) XRD of pure ZGO nanorods, pure PVDF fibers, and PVDF-ZGO fiber composites (1.25–10 wt % of nanorods).

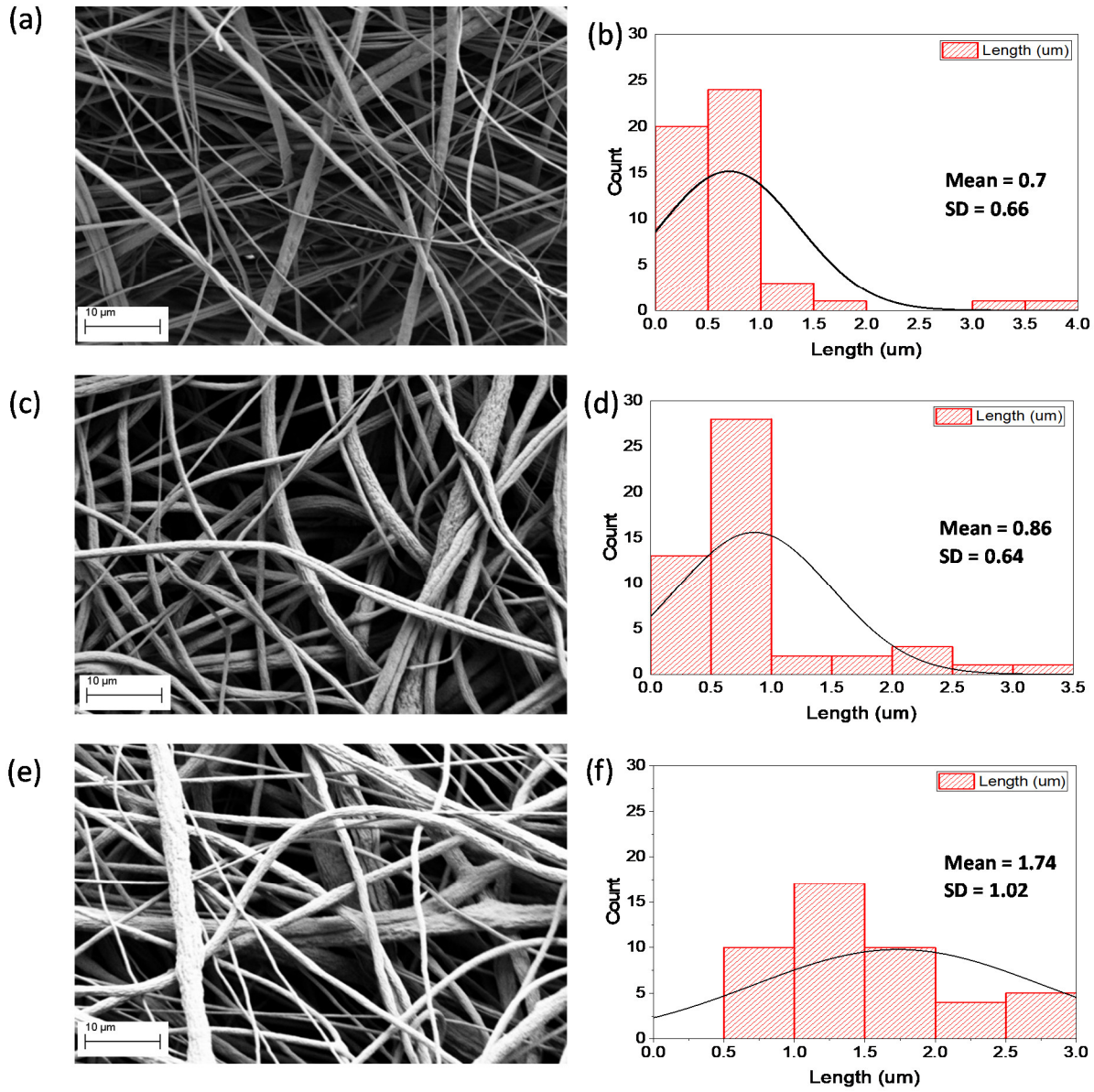

Figure 3. *Cont.*

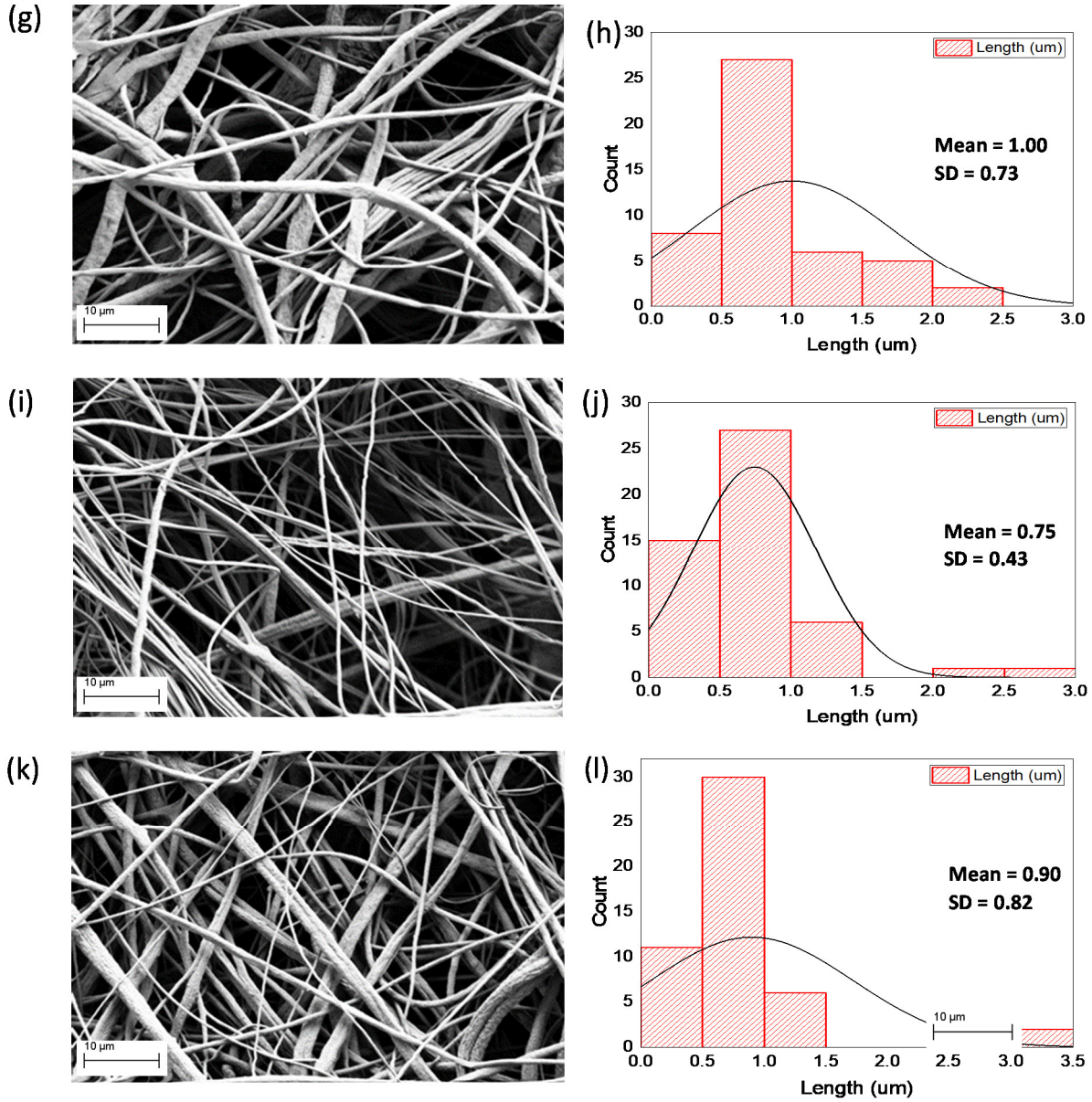

Figure 3. SEM morphology and corresponding histograms showing fiber diameter lengths of (**a**,**b**) PVDF fiber, (**c**,**d**) PVDF-1.25% ZGO, (**e**,**f**) PVDF-2.5% ZGO, (**g**,**h**) PVDF-3.75% ZGO, (**i**,**j**) PVDF-5% ZGO, and (**k**,**l**) PVDF-10% ZGO.

Figure 4a,b shows the digital image when the PVDF and PVDF-ZGO fiber mats were excited by a UV lamp under 302 nm of irradiation. While the PVDF fibers did not emit any color, the PVDF-ZGO fibers showed bluish-white uniform emission under a UV lamp. This confirms a homogenous distribution of the ZGO within the developed fibers. Figure 4c shows the PL excitonic emission spectra of the PVDF-ZGO systems. The photoluminescence excitation spectra display a broad emission range in the visible region of the spectrum for the PVDF-10 wt % ZGO fibers. The highest peak around 500 nm wavelength can be attributed to radiative recombination between the donor level containing oxygen vacancies and zinc interstitial and the acceptor level comprising zinc and germanium vacancies [52].

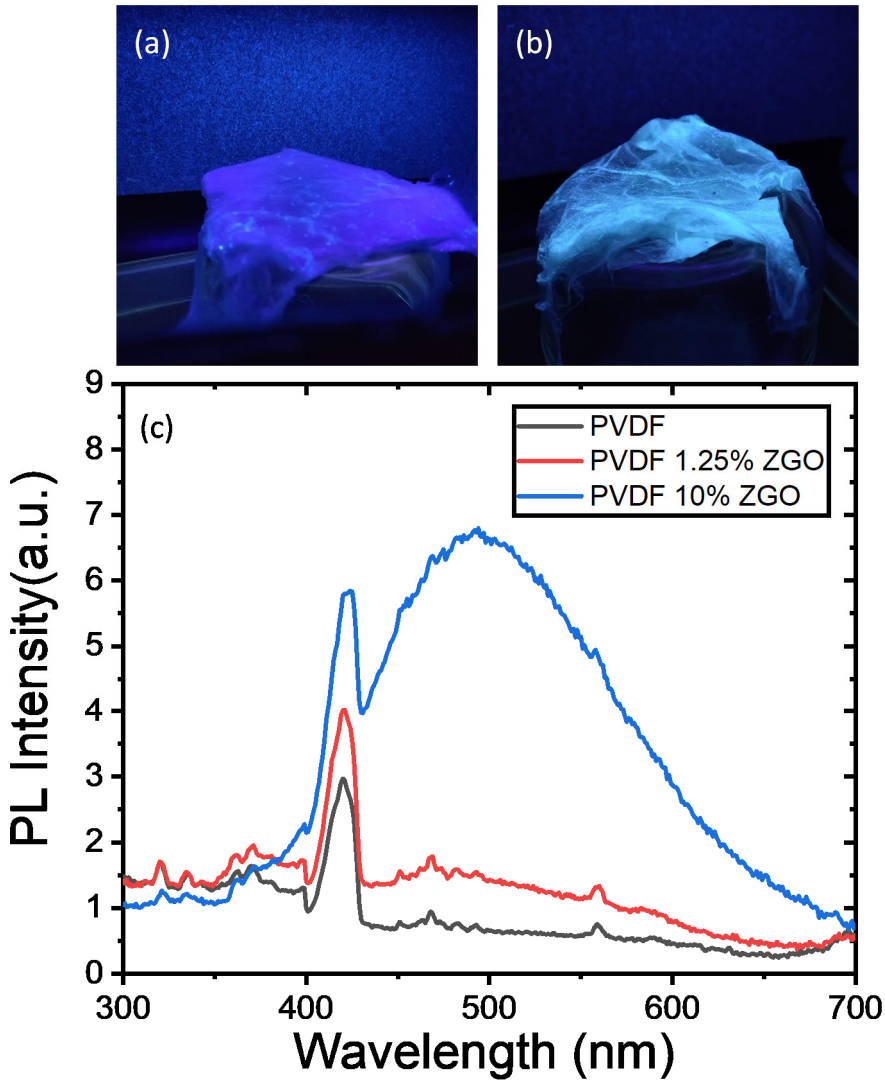

Figure 4. Digital image of (**a**) PVDF and (**b**) PVDF-ZGO fibers under UV lamp irradiation. (**c**) Photoluminescence excitation spectra of PVDF fiber mats with 1.25 wt % and 10 wt % ZGO loading.

The effect of ZGO fillers on the thermal stability of PVDF was analyzed through TGA analysis. The thermograms are shown in Figure 5. The main thermal degradation of the fibers is anticipated to be the result of two important parameters, the thermal degradation of the polymer PVDF as affected by the ZGO, and the thermal degradation of ZGO fillers. According to the thermogram, absorption of humidity can be considered negligible for all fiber composite systems. The main degradation of PVDF fiber initiated at 481 °C, and the fiber ended up with a residual mass of 26.6%. Some studies have shown that the presence of certain fillers improves the thermal stability of the polymer, mostly resulting from molecular pinning, which restricts movement and therefore increases the temperature needed to initiate molecular vibration; in some other studies, the presence of fillers speeds up thermal decomposition through their function as lubricants [53]. For the case of ZGO, it was observed that its addition results in decreased thermal stability. Polymer degradation started at 477, 446, 425, 413, and 336 °C for the 1.25, 2.5, 3.75, 5, and 10 wt % ZGO concentrations, respectively. The thermal degradation of the fibers can be better observed in the inset graph, which shows a magnified version of 350 to 450 °C vs. 80–90 wt % area. The residual mass for the PVDF-ZGO fibers also increased compared to the pure PVDF mats. The residual mass at 650 °C (once PVDF degraded) was 31.98% for the 1.25 wt % and 39.88% for the 10 wt % ZGO concentration.

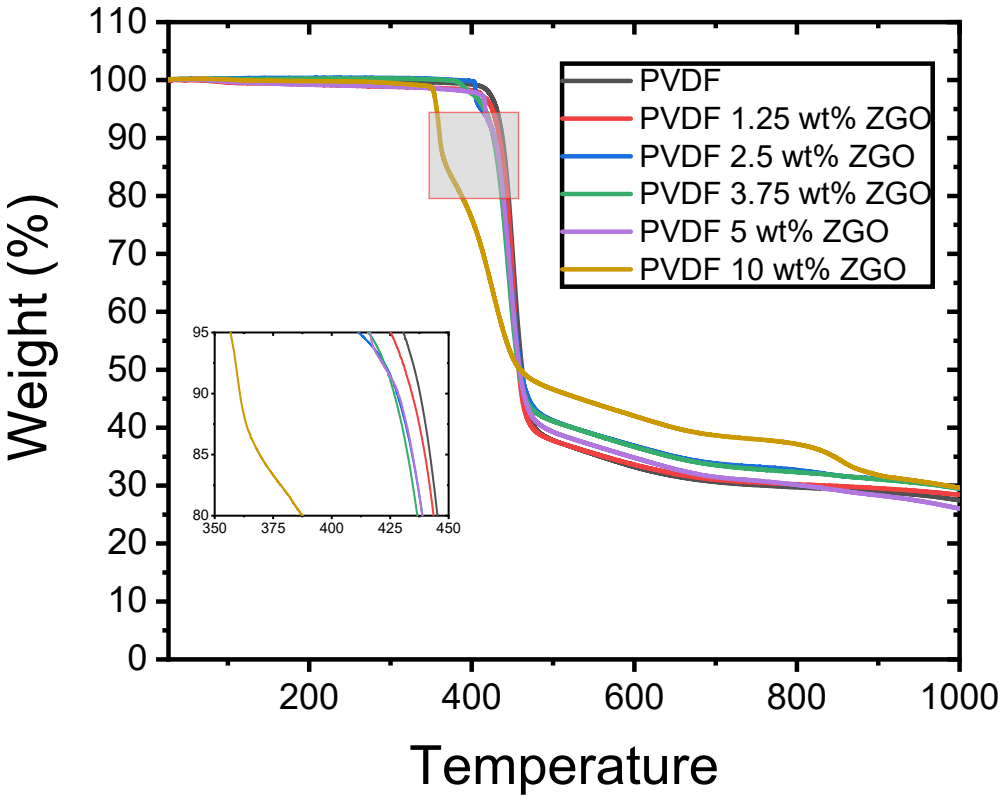

Figure 5. TGA curve for PVDF and PVDF-ZGO composite fibers.

Piezoelectric properties of the fiber composites were analyzed by measuring peak-to-peak output voltages when subjected to an external force. The mechanical stress can produce piezoelectric charges that create a potential difference between the sides of the copper plates acting as electrodes. When the mechanical stress in the form of pressure is applied, the external free charges will move to gather at the electrodes and a positive signal will be detected. When the stress is released, the potential difference between the two sides of the copper plate disappears. Hence, the accumulated charges flow back in the opposite direction, generating a negative electrical signal [54].

Figure 6 shows the highest output voltage generated by each of the fiber mats. The neat PVDF fibers generated an outstanding 144 V, which can be attributed to a higher fraction of the β phase and increased surface area. It was reported earlier that a higher fraction of the β phase results in a higher d_{33} piezoelectric coefficient, and thus a higher piezoelectric output [55]. The increase in5 surface area within the fiber mat also facilitates the free charges on the surface, which can be another factor for higher piezoelectric response. The resultant peak-to-peak output voltage for the fiber composites first increased to 172 V for the PVDF-1.25% ZGO fibers, which can be explained by the electrostatic interaction between the ZGO nanorods and PVDF. It can be assumed that the addition of the nanorods improved the polarization, which resulted in an enhanced alignment of the dipoles [50]. However, when the ZGO concentration was further increased from 2.5–10 wt %, the output voltage declined. This reduction in piezoelectric performance at higher reinforcement of NRs could be due to the outflow of charges through the conducting path of the electrodes and nanorods concentration reaching saturation for effective alignment [56]. It can also be explained similarly to results observed in ZnO nanowires [57], where the filler does not play a significant role in surface charge generation, and its initial contribution is mostly due to increasing the stress concentration near the PVDF fiber. Multiple studies have been conducted on pre-stressed and pre-polarized piezoelectric materials to further explain this phenomenon [58,59]. As observed in the XRD analysis, as the concentration of ZGO increases, the peaks of ZGO become more prominent, and this may have subdued the effect

of the β phase, resulting in a lower output voltage. Peak-to-peak voltage with respect to PVDF and PVDF-ZGO mats are further summarized in the histogram shown in Figure 6g. The histogram outlines the maximum, minimum, and average output voltage displayed by each fiber composite mat. The average piezoelectric response by PVDF-1.25% ZGO was 132 V, which is 25% higher than the average output voltage exhibited by pure PVDF fibers. Further increases in ZGO within the fiber composite showed a gradual declining of the peak-to-peak voltage response, down to an average peak-to-peak voltage of 59.6 V for the PVDF-10% ZGO fiber composite mat. Table 1 compares the results of the present study with similar PVDF-based composite systems.

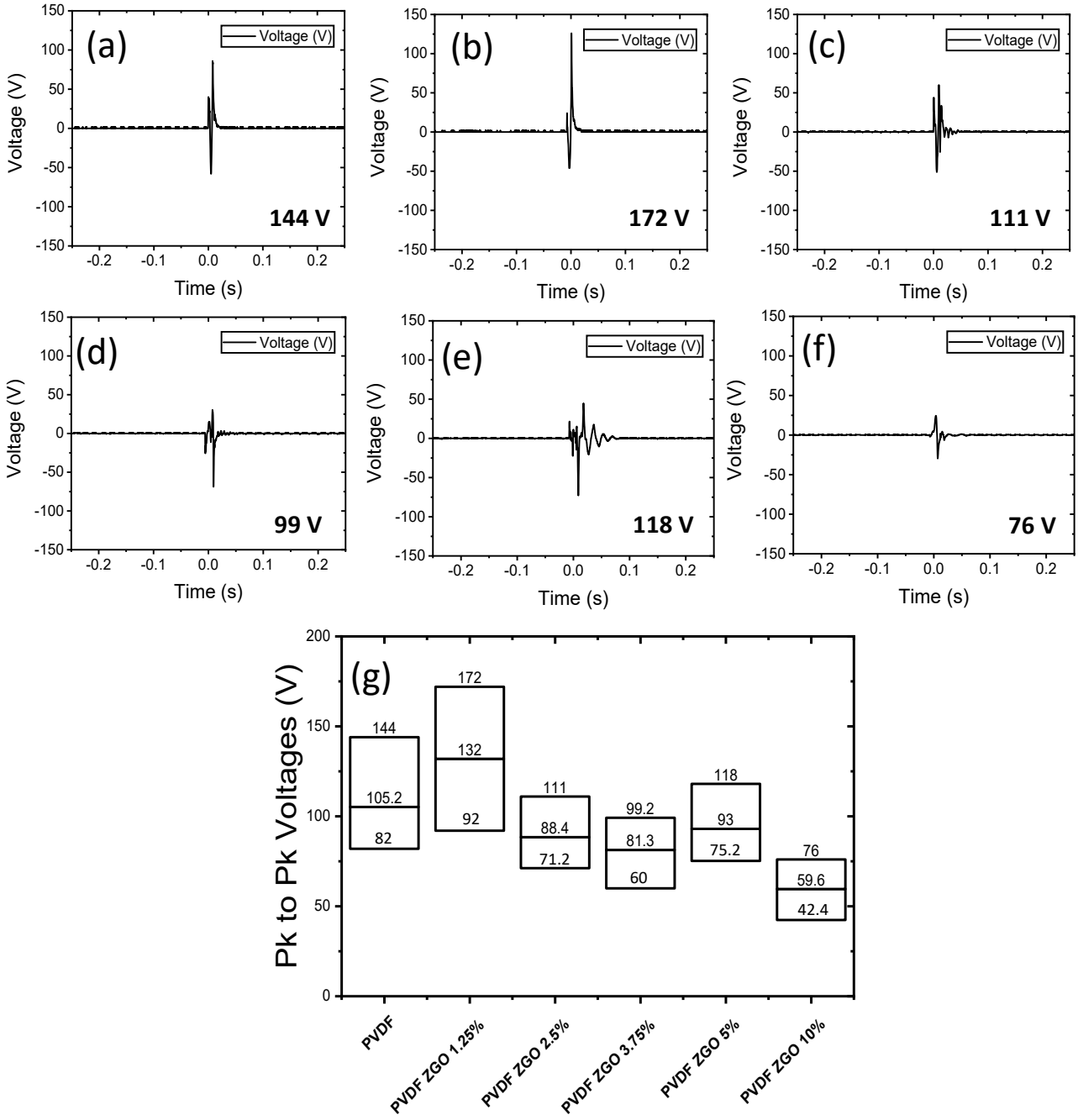

Figure 6. Highest peak-to-peak voltage produced during initial loading by (**a**) PVDF fiber, (**b**) PVDF-1.25 wt % ZGO, (**c**) PVDF-2.5 wt % ZGO, (**d**) PVDF-3.75 wt % ZGO, (**e**) PVDF-5 wt % ZGO, and (**f**) PVDF10 wt % ZGO; (**g**) histogram shows minimum, mean, and maximum peak-to-peak voltage produced by all fiber mat systems.

Table 1. Comparison of peak-to-peak results with similar PVDF-based composite systems.

Source	Material	Type	Testing Method	Results
Ponnamma et al. (2019) [60]	PVDF and $NiFe_2O_4$ and Ce-$NiFe_2O_4$ nanoparticles	Electrospinning	Mechanical loading	3–5 V
Bodkhe et al. (2017) [61]	PVDF and $BaTiO_3$	3D printed	Finger tapping	4 V
Parangusan et al. (2017) [24]	PVDF-HFP and Ni doped ZnO	Nanocomposite	Free vibration damping	1.2 V
Zhao et al. (2015) [62]	PVDF and $BaTiO_3$ NPs	Film	External load (1 Mpa)	150 V
Hu et al. (2018) [63]	PVDF and $BaTiO_3$ NPs	Film	External load	6.7 V
Issa et al. (2017) [35]	PVDF and Ag NP	Electrospun fibers	Mechanical vibration	0.6–2 V
Parangusan et al. (2019) [50]	PVDF and Ce–Fe_2O_3 and Ce–Co_3O_4	Electrospun fibers	External force	15–20 V
Samadi et al. (2019) [64]	PVDF and TiO_2-Fe_3O_4-MWCNT	Electrospun fibers	Finger tapping	51.42 mV
Chinya et al. (2020) [65]	PVDF/Polyaniline (PANI) in situ Ferrite nanorods	Film	Finger-friction motion	42 V
Pusty et al. (2019) [66]	PVDF and Ag doped rGO	Nanocomposite	Pulsing Mechanical energy	18 V
Karan et al. (2016) [67]	PVDF and AlO doped rGO	Nanocomposite	Mechanical energy	36 V
Roy et al. (2018) [68]	PVDF and CdS doped rGO	Electrospun fiber	Finger tapping	4 V
Cai et al. (2019) [69]	PVDF-HFP and Carbon black	Film	Resonance frequency	3.68 V
Singh et al. (2017) [70]	PVDF and $NaNbO_3$ nanorods and rGO	Nanocomposite	External load	2.16 V
Ponnamma et al. (2018) [71]	P(VDF-HFP) TiO_2-rGO nanotubes and $SrTiO_3$ nanoparticles	Nanocomposite film	External load	2 V
Ghosh et al. (2018) [72]	PVDF and Pt nanoparticles	Electrospun nanofiber	External load	30 V
Kar et al. (2019) [73]	PVDF and SnO_2 nanosheets	Nanocomposite		42 V
Present Study	PVDF and PVDF-1.25%ZGO	Finefibers	External load (206 kPa)	144 V and 172 V

4. Conclusions

In the present study, we developed and extensively characterized PVDF-ZGO fine fiber composite membranes. SEM micrographs showed long, continuous, and highly homogeneous fibers, with fiber diameter ranging between 0.7 and 1 μm depending on the ZGO concentration. XRD analysis depicted the presence of the ZGO and the expected α to β phase transition of the PVDF as the system was subjected to mechanical stretching for fiber formation. Photoluminescence excitation spectra showed a homogenous dispersion of the ZGO nanorods and a broad emission range in the visible region of the spectrum, with the highest peak around 500 nm for PVDF-10 wt % ZGO fibers. ZGO fillers negatively affected the thermal stability of the developed fiber composites by close to 100 °C for the sample containing 10 wt % of ZGO. The piezoelectric response was analyzed, and the highest peak-to-peak voltage was found for the PVDF-1.25 wt % ZGO, which showed a response of 172 V, which is 20% higher than the highest output voltage exhibited by pure PVDF fine fibers. This amplification of piezoelectric response can be attributed to a higher fraction of the β phase, enhanced alignment of the dipoles, surface charge generation, and increase in the stress concentration. Even though with increasing concentration of ZGO, the piezoelectric effect decreased, the lowest output voltage recorded was 42 V, which is still significantly high when compared to those reported in the literature. The developed fiber composite systems have promising energy harvesting and photoluminescence applications given their low cost, facile fabrication, and outstanding piezoelectric performance.

Author Contributions: Conceptualization, F.R. and K.L.; methodology, F.R., S.M., H.V. and B.B.S.; validation, F.R., S.M., B.B.S. and K.L.; formal analysis, F.R.; investigation, F.R. and B.B.S.; resources, K.L.; data curation, F.R., S.M. and B.B.S.; writing—original draft preparation, F.R., S.M. and K.L.; writing—review and editing, F.R., S.M., B.B.S., H.V. and K.L.; visualization, F.R. and S.M.; supervision,

K.L.; project administration, K.L.; funding acquisition, K.L. All authors have read and agreed to the published version of the manuscript.

Funding: This research was funded by National Science Foundation under DMR award PREM 2122178.

Institutional Review Board Statement: Not applicable.

Informed Consent Statement: Not applicable.

Acknowledgments: The authors gratefully acknowledge support received by National Science Foundation under DMR award PREM 2122178.

Conflicts of Interest: The authors declare no conflict of interest.

References

1. Zhu, J.; Zhu, Y.; Song, W.; Wang, H.; Gao, M.; Cho, M.; Park, I. Zinc oxide-enhanced piezoelectret polypropylene microfiber for mechanical energy harvesting. *ACS Appl. Mater. Interfaces* **2018**, *10*, 19940–19947. [CrossRef]
2. Wang, Z.L.; Wu, W. Nanotechnology-Enabled Energy Harvesting for Self-Powered Micro-/Nanosystems. *Angew. Chem. Int. Ed.* **2012**, *51*, 11700–11721. [CrossRef] [PubMed]
3. Sullivan, J.L.; Gaines, L. A review of battery life-cycle analysis: State of knowledge and critical needs. *Batter. Manuf. Electr. Hybrid Veh.* **2010**, 91–133. [CrossRef]
4. Das Mahapatra, S.; Mohapatra, P.C.; Aria, A.I.; Christie, G.; Mishra, Y.K.; Hofmann, S.; Thakur, V.K. Piezoelectric Materials for Energy Harvesting and Sensing Applications: Roadmap for Future Smart Materials. *Adv. Sci.* **2021**, *8*, 2100864. [CrossRef]
5. Bhavanasi, V.; Kusuma, D.Y.; Lee, P.S. Polarization orientation, piezoelectricity, and energy harvesting performance of ferroelectric PVDF-TrFE nanotubes synthesized by nanoconfinement. *Adv. Energy Mater.* **2014**, *4*, 1–8. [CrossRef]
6. Wang, H.; Xu, L.; Wang, Z. Advances of High-Performance Triboelectric Nanogenerators for Blue Energy Harvesting. *Nanoenergy Adv.* **2021**, *1*, 32–57. [CrossRef]
7. Karan, S.K.; Maiti, S.; Lee, J.H.; Mishra, Y.K.; Khatua, B.B.; Kim, J.K. Recent advances in self-powered Tribo-/Piezoelectric energy harvesters: All-In-One package for future smart technologies. *Adv. Funct. Mater.* **2020**, *30*, 2004446. [CrossRef]
8. Shan, X.; Tian, H.; Cao, H.; Xie, T. Enhancing Performance of a Piezoelectric Energy Harvester System for Concurrent Flutter and Vortex-Induced Vibration. *Energies* **2020**, *13*, 3101. [CrossRef]
9. Masara, D.O.; El Gamal, H.; Mokhiamar, O. Split Cantilever Multi-Resonant Piezoelectric Energy Harvester for Low-Frequency Application. *Energies* **2021**, *14*, 5077. [CrossRef]
10. Safaei, M.; Sodano, H.A.; Anton, S.R. A review of energy harvesting using piezoelectric materials: State-of-the-art a decade later (2008–2018). *Smart Mater. Struct.* **2019**, *28*, 113001. [CrossRef]
11. Erturk, A.; Bilgen, O.; Inman, D.J. Power generation and shunt damping performance of a single crystal lead magnesium niobate-lead zirconate titanate unimorph: Analysis and experiment. *Appl. Phys. Lett.* **2008**, *93*, 224102. [CrossRef]
12. Ren, B.; Or, S.W.; Zhang, Y.; Zhang, Q.; Li, X.; Jiao, J.; Wang, W.; Liu, D.; Zhao, X.; Luo, H. Piezoelectric energy harvesting using shear mode 0.71Pb (Mg1/3Nb2/3) O3–0.29PbTiO3 single crystal cantilever. *Appl. Phys. Lett.* **2010**, *96*, 083502. [CrossRef]
13. Shahab, S.; Zhao, S.; Erturk, A. Soft and hard piezoelectric ceramics and single crystals for random vibration energy harvesting. *Energy Technol.* **2018**, *6*, 935–942. [CrossRef]
14. Wu, M.; Zheng, T.; Zheng, H.; Li, J.; Wang, W.; Zhu, M.; Li, F.; Yue, G.; Gu, Y.; Wu, J. High-performance piezoelectric-energy-harvester and self-powered mechanosensing using lead-free potassium–sodium niobate flexible piezoelectric composites. *J. Mater. Chem. A* **2018**, *6*, 16439–16449. [CrossRef]
15. Zheng, M.; Hou, Y.; Yan, X.; Zhang, L.; Zhu, M. A highly dense structure boosts energy harvesting and cycling reliabilities of a high-performance lead-free energy harvester. *J. Mater. Chem. C* **2017**, *5*, 7862–7870. [CrossRef]
16. Qaiser, M.A.; Hussain, A.; Zhang, J.; Wang, Y.; Zhang, S.; Chen, L.; Yuan, G. 0–3 type Bi3TaTiO9:40wt%BiFeO3 composite with improved high-temperature piezoelectric properties. *J. Alloys Compd.* **2018**, *740*, 1–6. [CrossRef]
17. Li, Q.; Wei, J.; Cheng, J.; Chen, J. High temperature dielectric, ferroelectric and piezoelectric properties of Mn-modified $BiFeO_3$-$BaTiO_3$ lead-free ceramics. *J. Mater. Sci.* **2017**, *52*, 229–237. [CrossRef]
18. Wang, Z.L. Piezoelectric nanogenerators based on zinc oxide nanowire arrays. *Science* **2006**, *312*, 242–246. [CrossRef]
19. Mishra, S.; Unnikrishnan, L.; Nayak, S.K.; Mohanty, S. Advances in Piezoelectric Polymer Composites for Energy Harvesting Applications: A Systematic Review. *Macromol. Mater. Eng.* **2019**, *304*, 1–25. [CrossRef]
20. Hosseini, S.M.; Yousefi, A.A. Electrospun PVDF/MWCNT/OMMT hybrid nanocomposites: Preparation and characterization. *Iran. Polym. J.* **2017**, *26*, 331–339. [CrossRef]
21. Lang, C.; Fang, J.; Shao, H.; Ding, X.; Lin, T. High-sensitivity acoustic sensors from nanofibre webs. *Nat. Commun.* **2016**, *7*, 11108. [CrossRef]
22. Cheng, X.; Xue, X.; Ma, Y.; Han, M.; Zhang, W.; Xu, Z.; Zhang, H.; Zhang, H. Implantable and self-powered blood pressure monitoring based on a piezoelectric thinfilm: Simulated, in vitro and in vivo studies. *Nano Energy* **2016**, *22*, 453–460. [CrossRef]

23. Karan, S.K.; Maiti, S.; Agrawal, A.K.; Das, A.K.; Maitra, A.; Paria, S.; Bera, A.; Bera, R.; Halder, L.; Mishra, A.K.; et al. Designing high energy conversion efficient bio-inspired vitamin assisted single-structured based self-powered piezoelectric/wind/acoustic multi-energy harvester with remarkable power density. *Nano Energy* **2019**, *59*, 169–183. [CrossRef]
24. Parangusan, H.; Ponnamma, D.; AlMaadeed, M.A.A. Flexible tri-layer piezoelectric nanogenerator based on PVDF-HFP/Ni-doped ZnO nanocomposites. *RSC Adv.* **2017**, *7*, 50156–50165. [CrossRef]
25. Kang, S.J.; Park, Y.J.; Hwang, J.Y.; Jeong, H.J.; Lee, J.S.; Kim, K.J.; Kim, H.-C.; Huh, J.; Park, C. Localized pressure-induced ferroelectric pattern arrays of semicrystalline poly (vinylidene fluoride) by microimprinting. *Adv. Mater.* **2007**, *19*, 581–586. [CrossRef]
26. Ruan, L.; Yao, X.; Chang, Y.; Zhou, L.; Qin, G.; Zhang, X. Properties and applications of the β phase poly (vinylidene fluoride). *Polymer* **2018**, *10*, 228. [CrossRef]
27. Pan, H.; Na, B.; Lv, R.; Li, C.; Zhu, J.; Yu, Z. Polar phase formation in poly(vinylidene fluoride) induced by melt annealing. *J. Polym. Sci. Part B Polym. Phys.* **2012**, *50*, 1433–1437. [CrossRef]
28. Benz, M.; Euler, W.; Gregory, O.J. The Role of Solution Phase Water on the Deposition of Thin Films of Poly (vinylidene fluoride). *Macromolecules* **2002**, *35*, 2682–2688. [CrossRef]
29. Sencadas, V.; Gregorio, R.; Lanceros-Méndez, S. α to β phase transformation and microestructural changes of PVDF films induced by uniaxial stretch. *J. Macromol. Sci. Part B* **2009**, *48*, 514–525. [CrossRef]
30. Golzari, N.; Adams, J.; Beuermann, S. Inducing β phase crystallinity in block copolymers of vinylidene fluoride with methyl methacrylate or styrene. *Polymer* **2017**, *9*, 306. [CrossRef]
31. Martins, P.; Costa, C.M.; Lanceros-Mendez, S. Nucleation of electroactive β-phase poly (vinilidene fluoride) with $CoFe_2O_4$ and $NiFe_2O_4$ nanofillers: A new method for the preparation of multiferroic nanocomposites. *Appl. Phys. A Mater. Sci. Process* **2011**, *103*, 233–237. [CrossRef]
32. Mendes, S.F.S.; Costa, C.M.; Caparros, C.; Sencadas, V.; Lanceros-Méndez, S. Effect of filler size and concentration on the structure and properties of poly (vinylidene fluoride)/$BaTiO_3$ nanocomposites. *J. Mater. Sci.* **2012**, *47*, 1378–1388. [CrossRef]
33. An, N.; Liu, H.; Ding, Y.; Zhang, M.; Tang, Y. Preparation and electroactive properties of a PVDF/nano-TiO_2 composite film. *Appl. Surf. Sci.* **2011**, *257*, 3831–3835. [CrossRef]
34. Martins, P.; Costa, C.M.; Benelmekki, M.; Botelho, G.; Lanceros-Mendez, S. On the origin of the electroactive poly (vinylidene fluoride) β-phase nucleation by ferrite nanoparticles via surface electrostatic interactions. *CrystEngComm* **2012**, *14*, 2807–2811. [CrossRef]
35. Issa, A.A.; Al-Maadeed, M.A.; Luyt, A.S.; Ponnamma, D.; Hassan, M.K. Physico-Mechanical, Dielectric, and Piezoelectric Properties of PVDF Electrospun Mats Containing Silver Nanoparticles. *C* **2017**, *3*, 30. [CrossRef]
36. Maity, N.; Mandal, A.; Nandi, A.K. Hierarchical nanostructured polyaniline functionalized graphene/poly (vinylidene fluoride) composites for improved dielectric performances. *Polymer* **2016**, *103*, 83–97. [CrossRef]
37. Simoes, R.; Silva, J.; Vaia, R.; Sencadas, V.; Costa, P.; Gomes, J.; Lanceros-Mendez, S. Low percolation transitions in carbon nanotube networks dispersed in a polymer matrix: Dielectric properties, simulations and experiments. *Nanotechnology* **2008**, *20*, 035703. [CrossRef] [PubMed]
38. Sarkar, K.; Gomez, C.; Zambrano, S.; Ramirez, M.; de Hoyos, E.; Vasquez, H.; Lozano, K. Electrospinning to Forcespinning™. *Mater. Today* **2010**, *13*, 12–14. [CrossRef]
39. Comin, A.; Manna, L. New materials for tunable plasmonic colloidal nanocrystals. *Chem. Soc. Rev.* **2014**, *43*, 3957–3975. [CrossRef] [PubMed]
40. Sun, L.; Qi, Y.; Jia, C.-J.; Jin, Z.; Fan, W. Enhanced visible-light photocatalytic activity of g-C_3N_4/Zn_2GeO_4 heterojunctions with effective interfaces based on band match. *Nanoscale* **2014**, *6*, 2649–2659. [CrossRef]
41. Chen, D.; Wang, Q.; Wang, R.; Shen, G. Ternary oxide nanostructured materials for supercapacitors: A review. *J. Mater. Chem. A* **2015**, *3*, 10158–10173. [CrossRef]
42. Li, R.; Zhang, R.; Lou, Z.; Huang, T.; Jiang, K.; Chen, D.; Shen, G. Electrospraying preparation of metal germanate nanospheres for high-performance lithium-ion batteries and room-temperature gas sensors. *Nanoscale* **2019**, *11*, 12116–12123. [CrossRef]
43. Suzuki, V.Y.; Amorin, L.H.C.; Lima, N.M.; Machado, E.G.; Carvalho, P.E.; Castro, S.; Alves, C.C.S.; Carli, A.P.; Li, M.S.; Longo, E.; et al. Characterization of the structural, optical, photocatalytic and in vitro and in vivo anti-inflammatory properties of Mn^{2+} doped Zn_2GeO_4 nanorods. *J. Mater. Chem. C* **2019**, *7*, 8216–8225. [CrossRef]
44. Liao, C.-H.; Huang, C.-W.; Chen, J.-Y.; Chiu, C.-H.; Tsai, T.; Lu, K.-C.; Lu, M.-Y.; Wu, W.-W. Optoelectronic Properties of Single-Crystalline Zn_2GeO_4 Nanowires. *J. Phys. Chem. C* **2014**, *118*, 8194–8199. [CrossRef]
45. Zhou, J.; Zhang, W.; Zhao, H.; Tian, J.; Zhu, Z.; Lin, N.; Qian, Y. Growth of Bouquet-like Zn_2GeO_4 Crystal Clusters in Molten Salt and Understanding the Fast Na-Storage Properties. *ACS Appl. Mater. Interfaces* **2019**, *11*, 22371–22379. [CrossRef]
46. Li, H.-H.; Wu, X.-L.; Zhang, L.-L.; Fan, C.-Y.; Wang, H.-F.; Li, X.-Y.; Sun, H.-Z.; Zhang, J.; Yan, Q. Carbon-Free Porous Zn_2GeO_4 Nanofibers as Advanced Anode Materials for High-Performance Lithium Ion Batteries. *ACS Appl. Mater. Interfaces* **2016**, *8*, 31722–31728. [CrossRef] [PubMed]
47. Yan, C.; Lee, P.S. Crystallographic Alignment of ZnO Nanorod Arrays on Zn_2GeO_4 Nanocrystals: Promising Lattice-Matched Substrates. *J. Phys. Chem. C* **2010**, *114*, 265–268. [CrossRef]
48. Srivastava, B.B.; Gupta, S.K.; Li, Y.; Mao, Y. Bright persistent green emitting water-dispersible Zn_2GeO_4: Mn nanorods. *Dalton Trans.* **2020**, *49*, 7328–7340. [CrossRef] [PubMed]

49. Trevino, J.E.; Mohan, S.; Salinas, A.E.; Cueva, E.; Lozano, K. Piezoelectric properties of PVDF-conjugated polymer nanofibers. *J. Appl. Polym. Sci.* **2021**, *138*, 50665. [CrossRef]
50. Parangusan, H.; Ponnamma, D.; Almaadeed, M.A.A. Toward High Power Generating Piezoelectric Nanofibers: Influence of Particle Size and Surface Electrostatic Interaction of Ce–Fe_2O_3 and Ce–Co_3O_4 on PVDF. *ACS Omega* **2019**, *4*, 6312–6323. [CrossRef]
51. Abir, S.S.H.; Gupta, S.K.; Ibrahim, A.; Srivastava, B.B.; Lozano, K. Tunable CsPb (Br/Cl)3 perovskite nanocrystals and further advancement in designing light emitting fiber membranes. *Mater. Adv.* **2021**, *2*, 2700–2710. [CrossRef]
52. Gao, G.; Wondraczek, L. Near-infrared down-conversion in Mn^{2+}–Yb^{3+} co-doped Zn_2GeO_4. *J. Mater. Chem. C* **2013**, *1*, 1952–1958. [CrossRef]
53. Tavares, M.I.; Junior, A.W.; Neto, R.P. Evaluation of intermolecular interactions in the PHB/ZnO nanostructured materials. *J. Nanosci. Nanotechnol.* **2016**, *16*, 7606–7610. [CrossRef]
54. Park, K.-I.; Jeong, C.K.; Ryu, J.; Hwang, G.-T.; Lee, K.J. Flexible and large-area nanocomposite generators based on lead zirconate titanate particles and carbon nanotubes. *Adv. Energy Mater.* **2013**, *3*, 1539–1544. [CrossRef]
55. Gomes, J.; Nunes, J.; Sencadas, V.; Lanceros-Mendez, S. Influence of the β-phase content and degree of crystallinity on the piezo- and ferroelectric properties of poly (vinylidene fluoride). *Smart Mater. Struct.* **2010**, *19*. [CrossRef]
56. Tiwari, S.; Gaur, A.; Kumar, C.; Maiti, P. Enhanced piezoelectric response in nanoclay induced electrospun PVDF nanofibers for energy harvesting. *Energy* **2019**, *171*, 485–492. [CrossRef]
57. Choi, M.; Murillo, G.; Hwang, S.; Kim, J.W.; Jung, J.H.; Chen, C.-Y.; Lee, M. Mechanical and electrical characterization of PVDF-ZnO hybrid structure for application to nanogenerator. *Nano Energy* **2017**, *33*, 462–468. [CrossRef]
58. Craciun, E.-M.; Baesu, E.; Soós, E. General solution in terms of complex potentials for incremental antiplane states in prestressed and prepolarized piezoelectric crystals: Application to mode III fracture propagation. *IMA J. Appl. Math.* **2004**, *70*, 39–52. [CrossRef]
59. Craciun, E.; Rabaea, A.; Das, S. Cracks Interaction in a Pre-Stressed and Pre-Polarized Piezoelectric Material. *J. Mech.* **2020**, *36*, 177–182. [CrossRef]
60. Ponnamma, D.; Aljarod, O.; Parangusan, H.; Al-Maadeed, S. Reduction in piezoelectric voltage generation for the cerium doped nickel ferrite nanoparticles filled PVDF-HFP nanocomposites. *Results Phys.* **2019**, *13*, 102130. [CrossRef]
61. Bodkhe, S.; Turcot, G.; Gosselin, F.P.; Therriault, D. One-Step solvent evaporation-assisted 3D printing of piezoelectric PVDF nanocomposite structures. *ACS Appl. Mater. Interfaces* **2017**, *9*, 20833–20842. [CrossRef]
62. Zhao, Y.; Liao, Q.; Zhang, G.; Zhang, Z.; Liang, Q.; Liao, X.; Zhang, Y. High output piezoelectric nanocomposite generators composed of oriented $BaTiO_3$ NPs@PVDF. *Nano Energy* **2015**, *11*, 719–727. [CrossRef]
63. Hu, P.; Yan, L.; Zhao, C.; Zhang, Y.; Niu, J. Double-layer structured PVDF nanocomposite film designed for flexible nanogenerator exhibiting enhanced piezoelectric output and mechanical property. *Compos. Sci. Technol.* **2018**, *168*, 327–335. [CrossRef]
64. Samadi, A.; Ahmadi, R.; Hosseini, S.M. Influence of TiO_2-Fe_3O_4-MWCNT hybrid nanotubes on piezoelectric and electromagnetic wave absorption properties of electrospun PVDF nanocomposites. *Org. Electron.* **2019**, *75*, 105405. [CrossRef]
65. Chinya, I.; Sasmal, A.; Sen, S. Conducting polyaniline decorated in-situ poled Ferrite nanorod-PVDF based nanocomposite as piezoelectric energy harvester. *J. Alloys Compd.* **2020**, *815*, 152312. [CrossRef]
66. Pusty, M.; Sinha, L.; Shirage, P.M. A flexible self-poled piezoelectric nanogenerator based on a rGO–Ag/PVDF nanocomposite. *New J. Chem.* **2018**, *43*, 284–294. [CrossRef]
67. Karan, S.K.; Bera, R.; Paria, S.; Das, A.K.; Maiti, S.; Maitra, A.; Khatua, B.B. An approach to design highly durable piezoelectric nanogenerator based on self-poled PVDF/AlO-rGO flexible nanocomposite with high power density and energy conversion efficiency. *Adv. Energy Mater.* **2016**, *6*, 1601016. [CrossRef]
68. Roy, K.; Mandal, D. CdS decorated rGO containing PVDF electrospun fiber based piezoelectric nanogenerator for mechanical energy harvesting application. In *AIP Conference Proceedings*; AIP Publishing: New York, NY, USA, 2018; Volume 1942, p. 050125.
69. Cai, J.; Hu, N.; Wu, L.; Liu, Y.; Li, Y.; Ning, H.; Liu, X.; Lin, L. Preparing carbon black/graphene/PVDF-HFP hybrid composite films of high piezoelectricity for energy harvesting technology. *Compos. Part A Appl. Sci. Manuf.* **2019**, *121*, 223–231. [CrossRef]
70. Singh, H.H.; Singh, S.; Khare, N. Design of flexible PVDF/$NaNbO_3$/RGO nanogenerator and understanding the role of nanofillers in the output voltage signal. *Compos. Sci. Technol.* **2017**, *149*, 127–133. [CrossRef]
71. Ponnamma, D.; Erturk, A.; Parangusan, H.; Deshmukh, K.; Ahamed, M.B.; Al-Maadeed, M.A.A. Stretchable quaternary phasic PVDF-HFP nanocomposite films containing graphene-titania-$SrTiO_3$ for mechanical energy harvesting. *Emergent Mater.* **2018**, *1*, 55–65. [CrossRef]
72. Ghosh, S.K.; Mandal, D. Synergistically enhanced piezoelectric output in highly aligned 1D polymer nanofibers integrated all-fiber nanogenerator for wearable nano-tactile sensor. *Nano Energy* **2018**, *53*, 245–257. [CrossRef]
73. Kar, E.; Bose, N.; Dutta, B.; Banerjee, S.; Mukherjee, N.; Mukherjee, S. 2D SnO_2 nanosheet/PVDF composite based flexible, self-cleaning piezoelectric energy harvester. *Energy Convers. Manag.* **2019**, *184*, 600–608. [CrossRef]